Parametric Study and Modeling of PZT Based Wave Propagation Technique Related to Practical Issues in Monitoring of Concrete Curing

Yee Yan Lim[a*], Kok Zee Kwong[b], Willey Yun Hsien Liew[c], Ricardo Vasquez Padilla[d], Chee Kiong Soh[e]

[a]School of Environment, Science and Engineering, Southern Cross University. PO Box 157, Lismore NSW 2480, Australia. yee.lim@scu.edu.au

[b]Civil Engineering Program, Faculty of Engineering, University Malaysia Sabah, Jalan UMS, 88400 Kota Kinabalu, Sabah, Malaysia. charleskwongkz@gmail.com

[c]Mechanical Engineering Program, Faculty of Engineering, University Malaysia Sabah, Jalan UMS, 88400 Kota Kinabalu, Sabah, Malaysia. wyhliew@ums.edu.my

[d]School of Environment, Science and Engineering, Southern Cross University. PO Box 157, Lismore NSW 2480, Australia. ricardo.vasquez.padilla@scu.edu.au

[e]School of Civil and Environmental Engineering, Nanyang Technological University, 50 Nanyang Avenue, Singapore 639798. csohck@ntu.edu.sg

*Corresponding Author

Abstract

This paper presents a series of investigative studies, mainly parametric and numerical, into various issues related to the practical application of the wave propagation (WP) technique in monitoring of concrete curing using smart material (PZT). This paper is an extension of a range of experimental studies presented in the authors' recent publication. Coupled field finite element (FE) simulation of the PZT-structure interaction in WP technique is conducted on mortar and concrete specimens. Identification of the pressure wave (P-wave) and the surface wave (R-wave) velocities simulated in the FE model is attempted. Results are found to be matching closely with

the experiment. The verified FE model, together with the theoretical model are then used to perform parametric study on selected factors related to the practical application of the technique, in particular those uncontrollable in the experiment, including the dynamic modulus of elasticity, the Poisson's ratio and the damping coefficient. Further experimental and analytical studies on the effect of varying temperature and humidity are also presented. A semi-analytical model previously proposed by the authors is finally adopted to generate a strength calibration chart for concrete with different coarse aggregates. The theoretical and FE models are proven to be useful alternatives to the experiment, which can be used in future design and optimization of the PZT based WP technique in monitoring of concrete curing.

Keywords

Piezoelectric, Lead Zirconate Titanate (PZT), Practical Issues, Wave Propagation Technique, Monitoring of Concrete Curing, Finite Element Method, Wave Equation

1. Introduction

Accurate predictive models are essential for understanding an engineering problem domain and the behaviors of various structural systems. The developments of theoretical or analytical models with closed form mathematical equations are generally useful in providing strong physical insights into a particular engineering problem. However, their practical applications are often limited by their simplicity. Numerical models such as finite elements (FE) models are excellent alternative to the analytical models. Finite element method (FEM) enables the analyst to numerically evaluate a sufficiently close approximate solution for an engineering problem when analytical model is unavailable.

In the past two decades, various analytical and FE models have also been developed and studied in the field of smart piezoelectric based structural health monitoring (Giurgiutiu *et al.*, 2002; Annamdas and Soh, 2009; Annamdas and Radhika 2013; Wang and Zhu, 2011) for both electromechanical impedance (EMI) technique and wave propagation (WP) technique. Some of these studies are reviewed in the following sections.

1.1 Modeling of EMI Technique

The EMI technique employs a single smart piezoceramics transducer (PZT), acting as collocated actuator and sensor. The mechanically attached PZT transducer is dynamically excited by an alternating voltage. The vibrational force generated by the PZT patch under the converse piezoelectric effect can be transferred to the host structure. The corresponding structural response at different excitation frequency will modulate the electric current (admittance signatures) across the PZT patch. These admittance signatures carry information pertinent to the vibratory characteristics, such as stiffness, density and damping ratio of the host structure.

Thus far, various EMI based analytical models simulating the PZT–structure interactions have been developed by researchers such as Liang *et al.* (1996), Giurgiutiu and Zagrai (2000), Bhalla and Soh (2004), Annamdas and Soh (2007), Lim and Soh (2012), and Gresil *et al.* (2012).

On the other hand, the coupled field FE model is found to exhibits exceptional robustness (Liu and Giurgiutiu, 2007), capable of simulating damage (Lim and Soh, 2011; Djemana and Hrairi, 2016). In comparison to most of the previously studied models, either purely analytical through impedance-based modeling or semi-analytical through FE-based impedance modeling, the coupled field FE models are able to accurately simulate minor resonance peaks (Yang *et al.*,

2008) and exhibit higher accuracy in both magnitude and resonance frequency, especially in the higher frequency range (> 60 kHz) (Lim and Soh, 2014).

Wang *et al.* (2014) formulate a 3-D electromechanical impedance model that characterized the interaction between an embedded square PZT transducer and the host structure based on the effective impedance. The model is experimentally and numerically verified using a smart concrete cube with embedded square PZT transducer. A new methodology to monitor the compressive strength of concrete based on the effective mechanical impedance is proposed.

Lu *et al.* (2017) recently developed a novel EMI based model for strength development monitoring of cementitious materials. They overcame the shortcoming of lack of physical model in the conventional EMI based technique by introducing the concept of "Smart Probe". A 3-D coupled field FE model is also established to predict the admittance spectrum of the Smart Probe embedded in cementitious material (Lu *et al.*, 2018).

Up to date, various analytical based models simulating the PZT-structure interaction has been developed. However, most of these models focus on metallic structures such as aluminum and steel. Literatures on concrete structures are fairly limited.

1.2 Modeling of WP Technique

In the field of WP technique, surface bonded PZT transducer actuates the host structure through "in-plane strain coupling" (Yu, 2006). Its strong planar actuation predominantly generates Lamb wave or R-wave (surface wave). Lamb wave is usually dominant in thin metallic structure whereas R-wave is common in thick structure, such as concrete. In thick structure, weaker pressure wave (P-wave) is also simultaneously excited. These waves travel radially outwards on the plane at which the PZT transducer is attached. Recently, WP technique finds its

application in concrete structures, extending into concrete hydration and strength monitoring (Gu et al., 2006; Kong et al., 2013). Kong *et al.* (2013) have successfully investigated the three states (fluid state, transition state, and hardened state) of very early age concrete based on classification of the received electrical signal. Kong and Song (2017) conducted a comparative study to investigate the performance of monitoring the very early age cement hydration process by using P-wave and shear wave (S-wave).

Similar to the EMI technique, modeling performed and studied in this area, thus far, focused mainly on metallic structures. Moulin et al. (2000) present a modelling approach that couples the normal mode expansion method with the FEM to predict the surface displacement of Lamb waves in a composite plate excited from a source. The source of the Lamb waves is generated from both surface bonded and embedded piezoelectric transducer. The applicability of the model is validated with experimental study.

Giurgiutiu (2005) presents a model of one-dimensional plane harmonic Lamb waves tuning mechanism with piezoelectric transducer. Assuming perfect bonding conditions, the interfacial shear is concentrated at the ends (i.e. pin-force model). The harmonic displacement and strain field is obtained by using the residual theorem to evaluate the integral of the inverse Fourier transform. A solution for a generic expression of the interface shear stress distribution is obtained. Lamb wave modes tuning curves with varying frequency are derived and verified against experimental results.

Giurgiutiu (2007) presents a series of 1-D and 3-D modeling involving piezoelectric generated guided waves propagating in thin metallic strip. Both conventional FE and coupled field FE modeling are conducted. In the conventional simulation, prescribed harmonic displacements are applied to nodes located at the opposite ends of the piezoelectric transducer.

Axial waves (S_0 mode) and flexural waves (A_0 mode) are separately simulated and studied. Effectiveness of both types of waves in detecting cracks is compared. The coupled field FE modeling is considered as a more complete analysis as the coupling between piezoelectric transducer and the host structure is simulated. Sensor's electrical signatures could be directly produced. Good agreements between both analyses are generally found.

Song *et al.* (2008) conduct FE study to simulate the generation and the reception of R-wave in the concrete structure. They show that the R-wave induced by the piezoelectric actuator can be detected by the sensor in spite of a fairly large distance. The FE simulation result has been experimentally validated. The authors conclude that the R-wave excited by surface bonded PZT transducer generated stronger actuation and thus a more effective sensing, in comparison to the embedded transducer.

Lim *et al.* (2016) propose a WP based semi-analytical concrete strength evaluation model. Classical wave equations are used in conjunction with the P-wave and R-wave acquired from the WP technique to predict the physical properties of concrete, namely the dynamic modulus and the Poisson ratio. The WP technique is proven to be capable of predicting the strength of mortar and concrete with different water-to-cement ratio throughout the curing process. The performance of the PZT based WP technique is also found to be comparable to other conventional techniques, including the rebound hammer, the ultrasonic pulse velocity and the EMI techniques. Tian *et al.* (2017) developed a simple and effective absorption attenuation model of stress waves in concrete based on the Rayleigh damping model.

Kijanka *et al.* (2015) present a three-dimensional temperature-dependent model of surface-bonded PZT on Lamb wave propagation. The effect of temperature on Lamb wave actuation, propagation and sensing is investigated. Actuation and sensing properties of PZT for

various temperatures are studied through the electric field analysis. It is found that the temperature-dependent physical properties of PZT, bond layers and host structures significantly affected the amplitude and phase of Lamb wave responses.

In this paper, a complete coupled field FE simulation into the WP based PZT– concrete structure interaction is performed. Both P-wave and R-wave are identified from the sensor's electrical signatures. Selected experimental results for verification are initially reported in the studies recently conducted by the same authors (Lim *et al.*, 2017). Parametric studies are then conducted using both FEM and theoretical wave equations. Experimental and analytical studies on the effect of temperature and humidity are also presented. A semi-analytical model previously proposed by the authors (Lim *et al.*, 2016) is finally adopted to produce strength calibration charts for concrete specimens with different types of coarse aggregate.

2. Semi-analytical Model for Concrete Strength Evaluation

Thus far, most of the studies conducted on monitoring of concrete curing using WP technique are non-parametric in nature, relying heavily on stochastic or statistical approach (Gu *et al.*, 2006; Shin *et al.*, 2008) to correlate the electrical signals and the concrete strength.

Lim *et al.* (2016) recently propose a semi-analytical model capable of quantitatively relate the wave velocity obtained from the sensor's electrical signatures to the physical properties of the concrete. Theoretically, the relationship between the dynamic modulus of elasticity of a solid medium and the wave velocity in homogeneous and isotropic solids of infinite dimensions can be expressed as (Jones, 1962)

$$V_P = \sqrt{\frac{E_d(1-v)}{\rho(1+v)(1-2v)}} \quad (1)$$

$$V_R = \frac{0.87+1.12v}{1+v}\sqrt{\frac{E_d}{\rho}\frac{1}{2(1+v)}} \quad (2)$$

where, E_d = dynamic modulus of elasticity (kN/mm^2), v = Poisson's ratio, ρ = density (kg/m^3), V_P = velocity of P-wave (m/s), V_R = velocity of R-wave (m/s).

The dynamic modulus of elasticity and Poisson's ratio is then correlated to the strength through some empirical equations such as the one proposed in BS8110-2-1985 (British Standard, 1985):

$$E_d = k\sqrt{f_{cu}} \quad (3)$$

where f_{cu} = compressive strength (N/mm^2), k = curve fit proportionality constant.

Consequently the concrete strength can be correlated to the P-wave velocity and the R-wave velocity, through the following semi-empirical relationships (Lim *et al.*, 2016):

$$f_{cu} = \left(\frac{\rho {V_p}^2(1+v)(1-2v)}{k(1-v)}\right)^2 \quad (4a)$$

$$f_{cu} = \left[\frac{2\rho(1+v)\left(\frac{V_R(1+v)}{0.87+1.12v}\right)^2}{k}\right]^2 \quad (4b)$$

where f_{cu} = compressive strength (N/mm^2), k = curve fit proportionality constant.

The advantage of this model lies in the fact that, it could theoretically derives the dynamic modulus of elasticity and Poisson's ratio of the concrete host structure with a single set of equipment and a single measurement, as both P-waves and R-waves velocities can be simultaneously measured through the WP technique.

3. Finite Element Simulation

In this study, commercial software package ANSYS 14.0 was used to simulate the PZT–structure smart system interaction. Coupled field analysis with piezoelectric inclusion was adopted, which allowed the modeling of both actuator and sensor. Piezoelectric analysis caters

for the interaction between structural and electric fields. The piezoelectric analysis makes use of the direct coupling method, involving one analysis with the use of one coupled-field element containing all necessary degrees of freedom.

In spite of the fact that inclusion of the PZT transducer into the FE models made the analysis more complicated, this complete modeling technique would yield a more accurate result especially at high frequency of excitation (Lim and Soh, 2014). In addition, the electrical sensor's signatures can be directly obtained from the simulation, resembling the results acquired from the experiment.

3.1 Modeling of PZT-Concrete Structure Interaction

Solid 45 element with eight nodes and three DOFs at each node was used to model the mortar or the concrete structure. SOLID 5 element was used to simulate the PZT transducer. SOLID 5 element is a coupled field element with eight nodes and up to six DOFs at each node. The additional DOFs in this coupled field element is the electrical voltage. The properties of the PZT patch, in accordance to PIC 151 (PI Ceramic, 2016) and the materials property of concrete are tabulated in Table 1 and Table 2, respectively.

Table 1. Properties of PIC 151 (PI Ceramics, 2016)

Parameters	**Symbols**	**Values**	**Unit**
Density	ρ	7800	kg/m^3
Dielectric loss factor	$tan\ \delta$	0.02	--
Compliance	s_{11}	15.0	$x\ 10^{-12}\ m^2/N$
	$s_{22} = s_{33}$	19.0	

	$s_{12} = s_{21}$	-4.50	
	$s_{13} = s_{31}$	-5.70	
	$s_{23} = s_{32}$	-5.70	
	$s_{44} = s_{55}$	39.0	
	s_{66}	49.4	
Electric Permittivity	ε_{11}^{T}	1.75	x 10^{-8} F/m
	ε_{22}^{T}	1.75	
	ε_{33}^{T}	2.12	
PZT Strain Coefficients	d_{31}	-2.10	x 10^{-10} m/V or x 10^{-10} C/N
	d_{32}	-2.10	
	d_{33}	5.00	
	d_{24}	5.80	
	d_{15}	5.80	

Table 2. Material properties of mortar or concrete

Parameters	**Symbols**	**Values**	**Unit**
Density	ρ	2180	kg/m^3
Poisson ratio	ν	0.27 (mortar) 0.26 (concrete)	
Young's modulus (Isotropic)	E	20.2 (mortar) 23.2 (concrete)	x 10^9 N/m^2
Constant stiffness multiplier	β	1.5 x 10^{-8}	

According to the study conducted by Song et al. (2008), concrete was assumed as a viscoelastic and isotropic material. Despite the fact that concrete is non-homogeneous due to the presence of coarse aggregate, this assumption gave a reasonably close estimate of the behavior of the system which remains useful for engineering application.

In order to further verify this observation, FEA (finite element analysis) is first conducted on mortar specimen (experiment: Specimen CaM) and then on concrete specimen (experiment: Specimen CaS) (refer to Table 1 of Lim *et al*., 2017). This is due to the fact that in comparison to concrete, the nature of mortar is closer to a homogeneous material. The accuracy of both simulations are then compared and discussed.

Rayleigh damping is used in this case, where mass and stiffness damping are considered to compensate the effects of the microstructure (Wu and Chang, 2006; Luo and Rose, 2007). The Rayleigh damping matrix can be expressed in terms of the stiffness, *S* and mass, *m* matrix as:

$$[C] = \alpha[m] + \beta[S] \quad (5)$$

where

α = constant mass damping multiplier

β = constant stiffness damping multiplier (Rayleigh damping)

The mass damping multiplier, α dominates the lower frequencies and the stiffness damping multiplier, β works better in the higher frequency range. In this study, the contribution from α is negligible as the frequencies used are in the higher frequency range (> 30 kHz). Therefore, α is taken as zero in this simulation. On the other hand, β determines the damping which is related to the material viscosity and proportional to the stain rate. In this study, β is determined through trial and error to achieve a best match with the experiment.

The mortar or concrete prism sized, 100 mm x 100 mm x 500 mm used in the experiment presented in Lim *et al.* (2017) was numerically simulated in this study. Simulating the full size of the structure in FEM is computationally intensive. In order to reduce the computation time, transmitting boundary (Balendra, 2005; Song *et al.*, 2008) is adopted on lateral planes to reduce the number of elements required. It could effectively suppress reflection at the boundaries of the computational field. In this case, the transmitting boundary is modeled as a thin layer (1 mm) of material with high damping ratio (β = 1) at both ends of the PZT transducers, as shown in Figure 1.

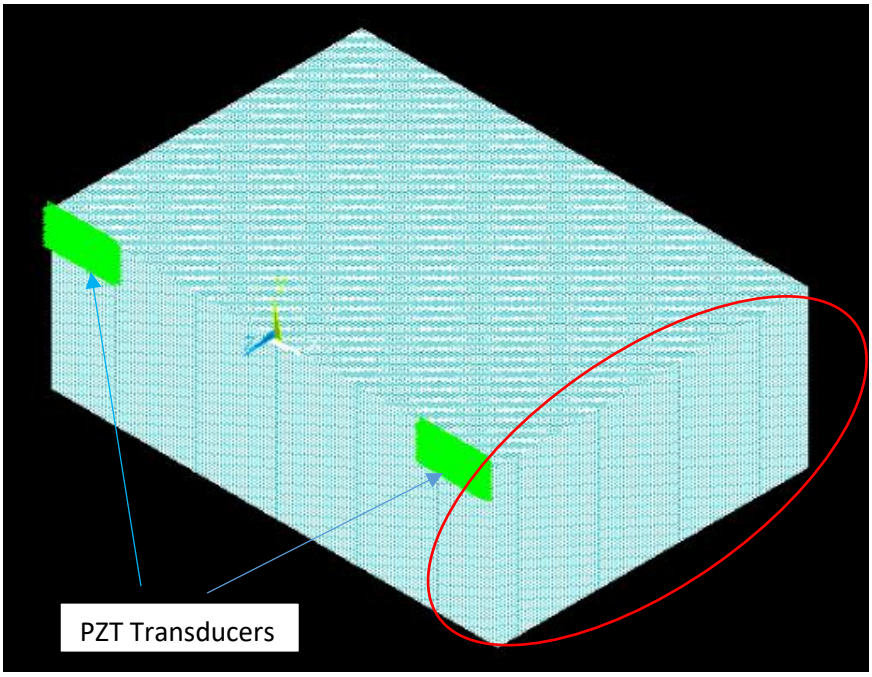

Figure 1. FE model of PZT-concrete structure interaction (1 mm thick transmitting boundaries at both ends, circled in red) simulated in ANSYS 14.0

Taking advantage of symmetry in geometry and loading condition, only half of the concrete beam, along the width direction was simulated. The size of the concrete beam was

eventually reduced to 50 mm in width, 100 mm in depth and 120 mm in length. One node at the center of the concrete beam was restrained in the *z*-direction (along the direction of depth) to maintain stability.

Following the experimental study presented in Lim *et al.* (2017), two PZT transducers (15 mm x 15 mm x 0.25 mm) spaced 100 mm apart were "bonded" to the surface of the mortar or concrete beam by coupling the displacement of the interfacial nodes.

For simplicity, the bonding layer between the PZT transducer and the structure is omitted in the simulation. The bonding layer is known to affect mainly the magnitude of the sensor's electrical signatures. According to the classical wave theory, the velocity of the elastic wave travelling in a medium is predominantly determined by the density, stiffness and Poisson's ratio of the medium. The presence of bonding layer between the PZT patch and the medium mainly reduce the amount of energy transferred to the medium due to shear lag effect but it will not change the mechanical properties (density, stiffness and Poisson's ratio) of the medium (Yang *et al*., 2008; Lim and Soh, 2014).

To minimize the effect of bonding on the acquired electrical signatures, the thickness of the glue was controlled in the experiment by applying uniform pressure across the PZT, ensuring uniform and thin bonding. 5-peaks sinusoidal tone burst of peak-to-peak 150 V was applied on the PZT actuator at 120 kHz.

3.2 Convergence of Solution

The size of the elements adopted should be sufficiently small to ensure reasonable accuracy of the solution, but at the same time should not be unnecessarily small to avoid unduly

long computation. According to Song *et al*. (2008), there should be at least ten elements per wavelength along the wave propagating direction.

In this study, convergence of solution is tested by performing several analyses on the same model, each time reducing the size of the mesh. The analysis starts with an element size of 2 mm, which was then reduced to 1 mm and 0.5 mm. The outcome is presented in Figure 2.

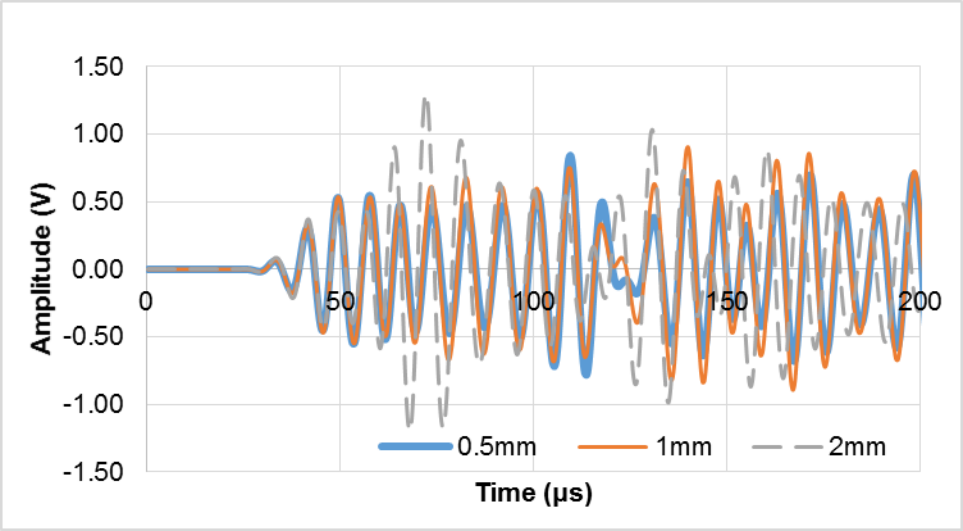

Figure 2. Numerically simulated sensor's electrical signatures against time for convergence test

The waveform and amplitude, for both 1 mm and 0.5 mm, are overlapping each other, indicating that the solution was converging. Hence, it can be deduced that element sized 1 mm is sufficiently fine for modeling the PZT-concrete interaction at 120 kHz. This observation aligned with Song *et al.* (2008), who also recommend 1 mm or 0.5 mm mesh size for WP technique on concrete structure with PZT actuation less than 200 kHz. In this study, 1 mm element is adopted.

3.3 Experimental Verification

To verify the accuracy of the FE model, the results are compared to the experimental results.

3.3.1 Mortar

Figure 3 depicts a comparison of sensor's electrical signatures between experiment and FE simulation of mortar specimen (Specimen CaM after 28 days of curing). In the FE simulation, the modulus of elasticity and Poisson ratio are found to 20.2 GPa and 0.27, respectively.

The velocities of both P-wave and R-wave are evaluated from the time of flight (TOF) of the P-wave and the R-wave packets, at known actuator-sensor spacing. Cross correlation analysis is adopted to enhance the accuracy of TOF. The details of such analysis can be found in Lim *et al.* (2017).

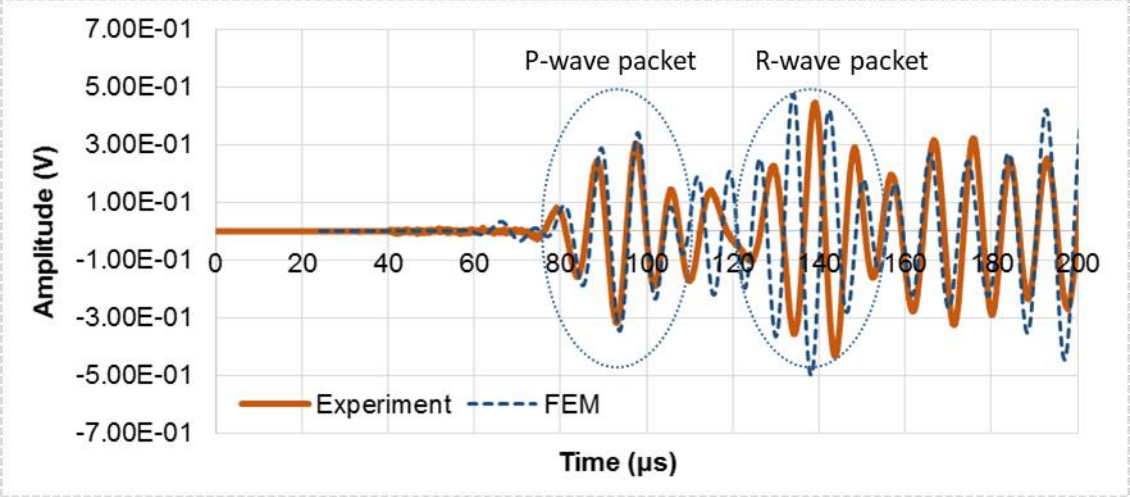

Figure 3. Sensor's electrical signatures against time obtained from experiment (Specimen CaM) and FE simulation (120 kHz)

A reasonably good agreement can be observed between the two, especially on the arrival of the first wave packet (P-wave), as shown in Figure 3. The P-wave velocities are 2612.5 m/s and 2580.4 m/s for the experiment and FE simulation, respectively.

In terms of the second wave packet (R-wave), its arrival based on the FE simulation is earlier than the experiment. The R-wave velocities are 1510.7 m/s and 1738.6 m/s for the experiment and FE simulation, respectively.

The minor variation is likely to be caused by the inherent roughness of the actual test specimen. Some imperfection on the surface of the test specimen, including small voids is observed, thus slowing the R-wave, which travels predominantly across the surface. The FE model, on the other hand, assumes a perfectly smooth surface. In addition, the inherent assumption of the numerical analysis could also be one of the causes for such variation.

Due to the uncertain nature of damping, trial and error is performed in the simulation to match the experimental results. β is finally found to be approximately 1.5×10^{-8}, which agrees closely with the value adopted by Song *et al.* (2008). Note that Figure 2 differed from Figure 3 as a smaller size model was adopted for the convergence test to reduce computational time.

3.3.2 Concrete

A comparison has also been made between experiment and FE simulation of concrete specimen with coarse aggregate (Figure 4). The experimental results are obtained from Specimen CaS (specimen with sandstone as the coarse aggregate) at 28 days, as presented in Lim *et al.* (2017). In the FE simulation, the modulus of elasticity and Poisson ratio are found to be 23.2 GPa and 0.26, respectively. The P-wave velocities are 2997.8 m/s and 3001.5 m/s for the

experiment and FE simulation, respectively. The R-wave velocities are 1712.3 m/s and 1719.5 m/s for the experiment and FE simulation, respectively.

Observing Figure 4, it can be deduced that reasonably good agreement is observed between the experiment and the FE simulation, indicating that assuming concrete as homogeneous material in the FE simulation yields close enough approximation of the actual behavior of the wave propagation in concrete medium. This observation is similar to the outcome presented in Song et al. (2008).

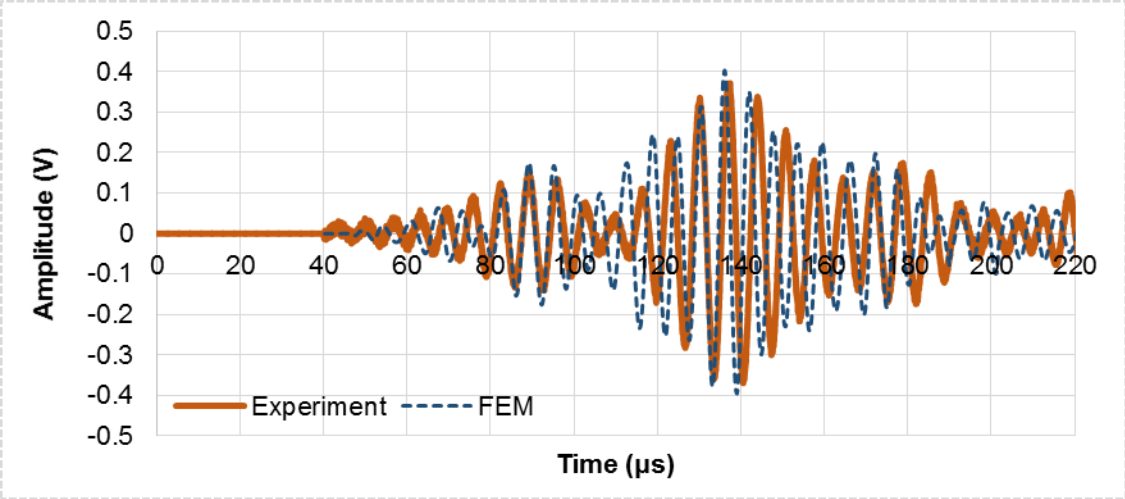

Figure 4. Sensor's electrical signatures against time obtained from experiment (Specimen CaS) and FE simulation (200 kHz)

However, it should be noted that this result should not be carelessly generalized considering the fact that random distribution of coarse aggregate within the concrete specimen cannot be accurately reflected in the simulation. In particular, the presence of coarse aggregate could potentially cause scattering of wave which induces more complex waveform. Further study should be conducted to achieve an in-depth understanding into this issue.

4. Parametric Study

In this section, a series of parametric studies are performed using the FEM and the analytical model to complement the experimental studies conducted by Lim *et al.* (2017).

The effect of varying the dynamic modulus of elasticity, Poisson's ratio and structural damping on the sensor's electrical signatures are first investigated. The effects of changing actuation waveform and actuation frequency are also conducted to verify the experimental results.

To reduce the computational time of the FE simulation, the analysis is performed on a smaller concrete beam, sized 20 mm x 120 mm x 50 mm. The sizes of PZT transducers (15 mm x 15 mm x 0.25 mm) and spacing (100 mm) remain the same.

4.1 Dynamic Modulus of Elasticity

Parametric study is first conducted by varying the dynamic modulus of elasticity, from 10 GPa to 40 GPa for each analysis, while withholding the rest of the properties.

Figure 5 shows the outcome of the simulation, in terms of amplitude of the sensor's electrical signature against time. The P-wave packets and R-wave packets can be easily identified between 10 GPa to 30 GPa (Figure 5a to Figure 5c). On the other hand, the sensor's electrical signature 40 GPa has shown relatively complicated wave packet (Figure 5d), indicating higher wave reflection intensity in a stiffer medium.

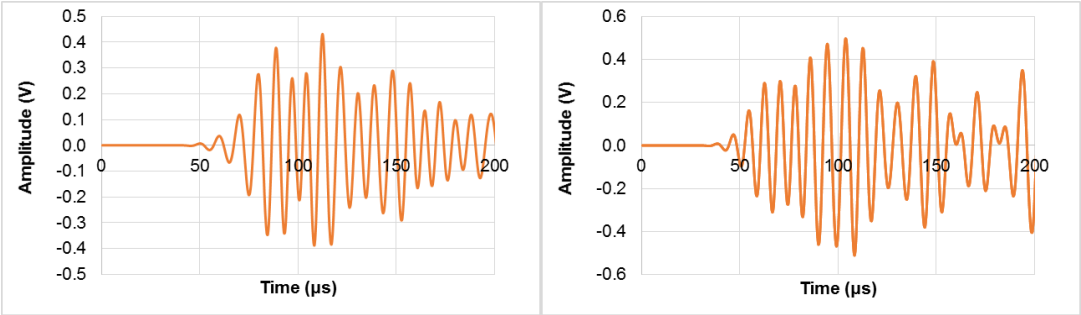

(a) 10 GPa

(b) 20 GPa

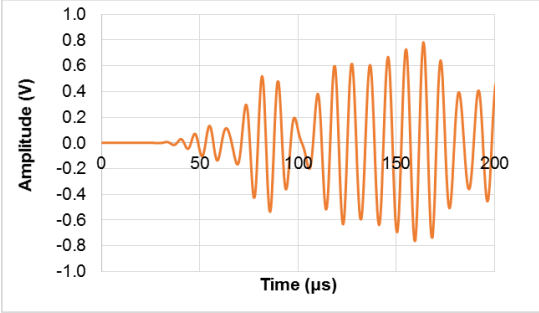

(c) 30 GPa

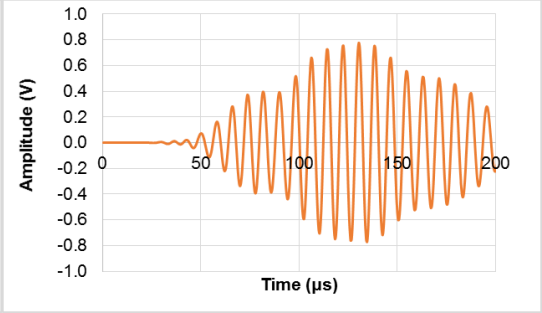

(d) 40 GPa

Figure 5. Sensor's electrical signatures against time of varying dynamic modulus of elasticity (10 GPa - 40 GPa) from FE simulation

Figure 6(a) illustrates the largest peak-to-peak amplitude of the sensor's electrical signature with different modulus of elasticity. The results show that the amplitude of the wave packet is proportional to the stiffness of the medium, indicating that energy absorption/dispersion is lower in stiffer medium.

Figure 6(b) presents the velocities of P-wave and R-wave obtained from the FE simulation. The wave velocities increase with the modulus of elasticity, which is in line with the structural dynamic theory.

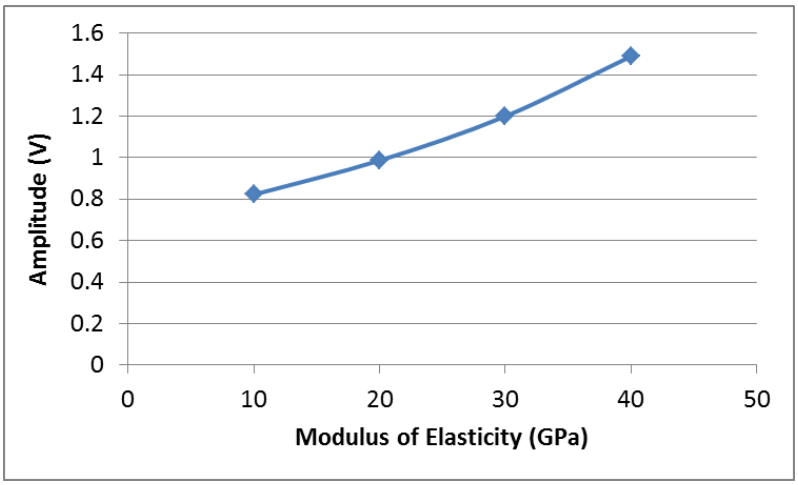

(a)

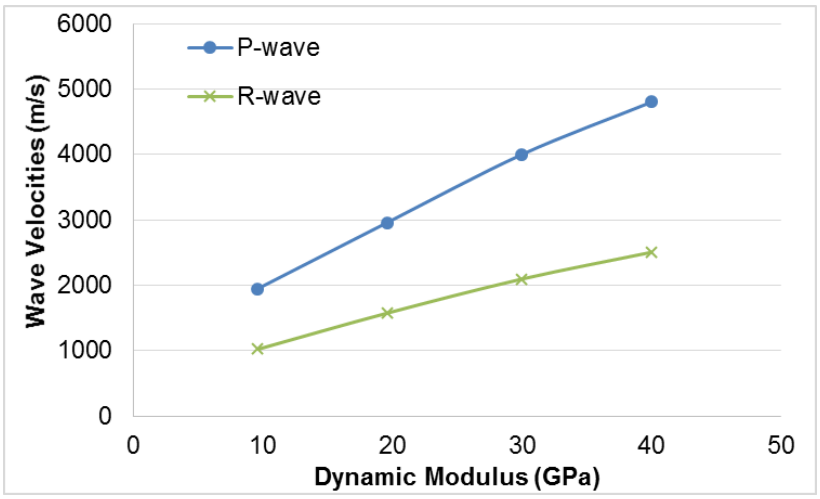

(b)

Figure 6. (a) Amplitudes and (b) wave velocities against dynamic modulus of elasticity (10 GPa - 40 GPa) from FE simulation

4.2 Poisson's Ratio

Poisson's ratios are varied from 0.1 to 0.5 while other parameters remain unchanged. Figure 7 shows the simulated sensor's electrical signature with different Poisson's ratio.

Figure 8(a) shows that the amplitude of the sensor's electrical signature generally increases with the Poisson's ratio. Figure 8(b) presents the velocities of P-wave and R-wave with varying Poisson's ratio from the theoretical model (Equation 1 and 2).

The P-wave velocity increases exponentially with the Poisson ratio, whereas the R-wave velocity remains predominantly constant. In this case, the theoretical model is adopted instead of the FE model as part of the results obtained from FE model is unstable. This is potentially caused by the fact that the extreme Poisson's ratio adopted in the FE simulation induces numerical error in the solution process, considering linear elastic analysis is assumed. Further study is required to investigate into these scenarios using more complex analysis.

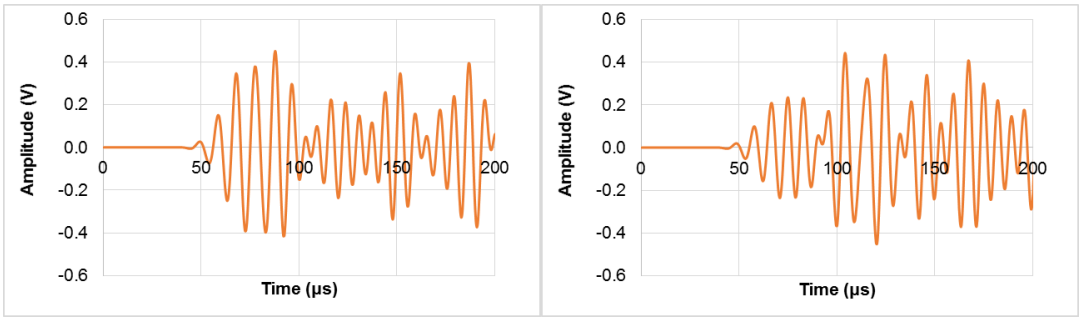

(a) 0.1 (b) 0.15

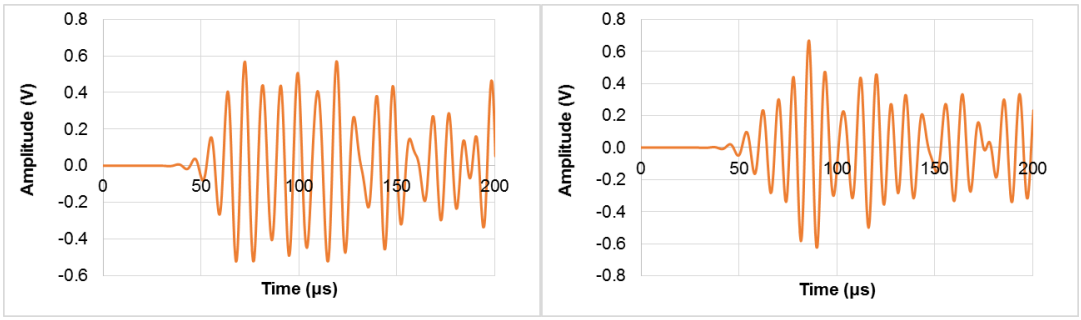

(c) 0.25 (d) 0.3

Figure 7. Sensor's electrical signatures against time of varying Poisson's ratio (0.1 to 0.3) from FE simulation

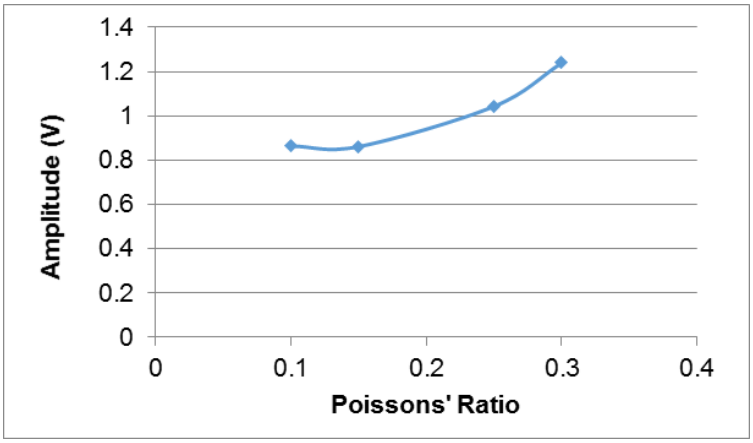

(a)

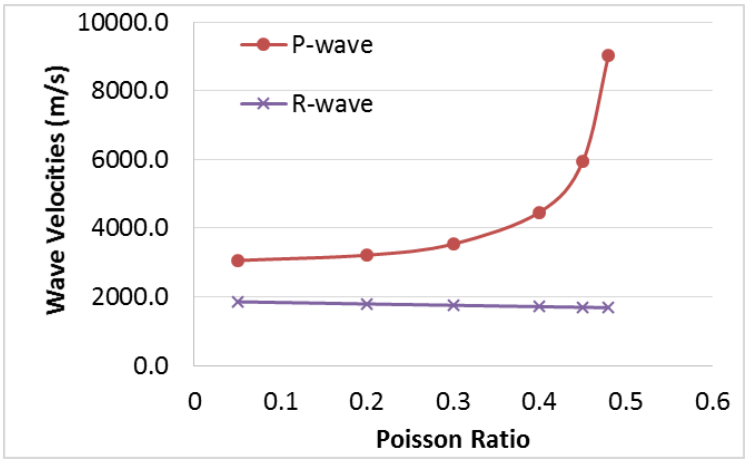

(b)

Figure 8. (a) Amplitudes (FEM) and (b) wave velocities (theory) against Poisson's ratio (0.05 – 0.5)

4.3 Structural Damping

To investigate the effect of damping ratio, specifically the constant stiffness damping multiplier, β, it is varied from 1.5 x 10^{-5} to 1.5 x 10^{-9}. Figure 8 shows the sensor's electrical signatures generated from the simulation.

It is noticed that the travel distance of actuation wave is significantly limited in a medium with β ranging between 1.5 x 10^{-6} to 1.5 x 10^{-5} due to overly high damping effect. Magnitudes of the sensor's electrical signatures are too low for both cases to yield any useful outcome (Figure

9a and 9b). When β is smaller than or equal to 1.5 x 10^{-7}, the wave packets of P-wave and R-wave start to appear (Figure 9c, 9d and 9e).

Figure 10a shows the largest peak-to-peak amplitudes and wave velocities of the sensor's electrical signatures against changing β. The amplitudes of the electrical signatures reduce sharply with increase in β, indicating that the energy dissipation or absorption is much higher on medium with higher damping.

The velocities of both P-wave and R-wave remain predominantly constant with β ranging from 1.5 x 10^{-7} to 1.5 x 10^{-9}, as shown in Figure 10(b). This outcome agree well with the structural dynamic theory, which states that the wave velocity are practically independent of damping.

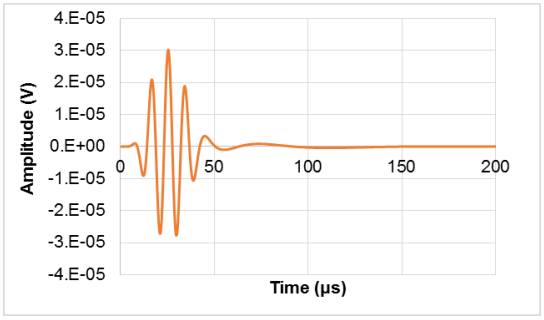

(a) 1.5 x 10^{-5}

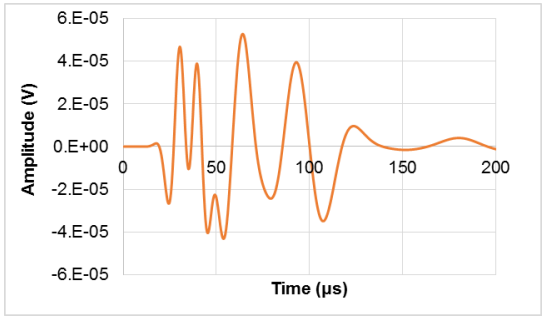

(b) 1.5 x 10^{-6}

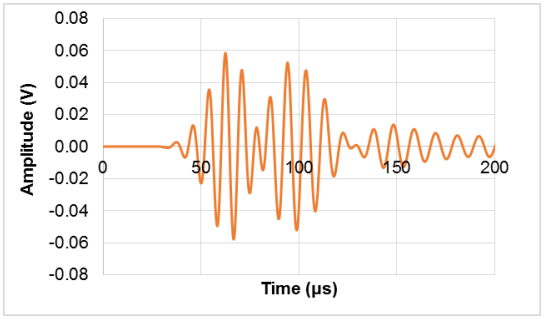

(c) 1.5 x 10^{-7}

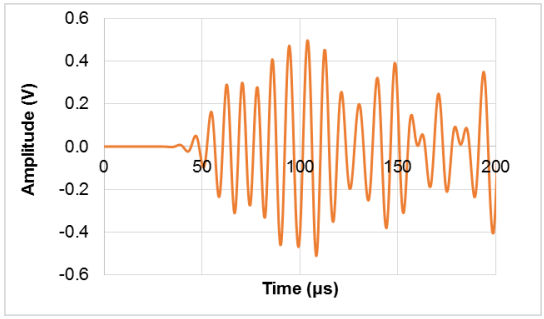

(d) 1.5x 10^{-8}

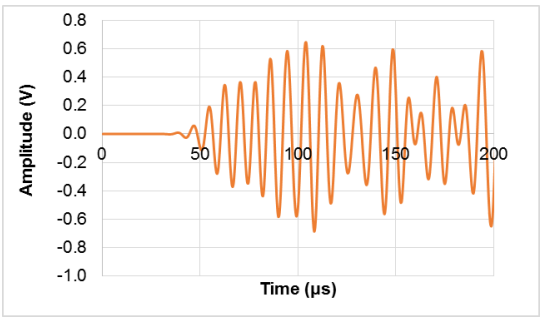

(e) 1.5x 10^{-9}

Figure 9. Sensor's electrical signatures against time for varying stiffness damping multiplier, β (1.5 x 10^{-5} - 1.5 x 10^{-9}) from FE simulation

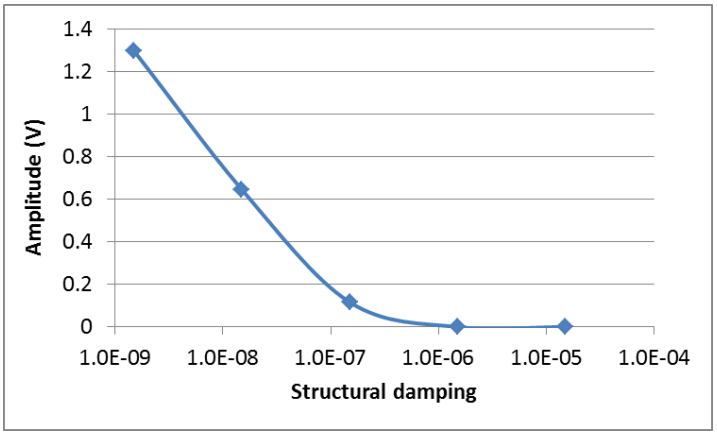

(a)

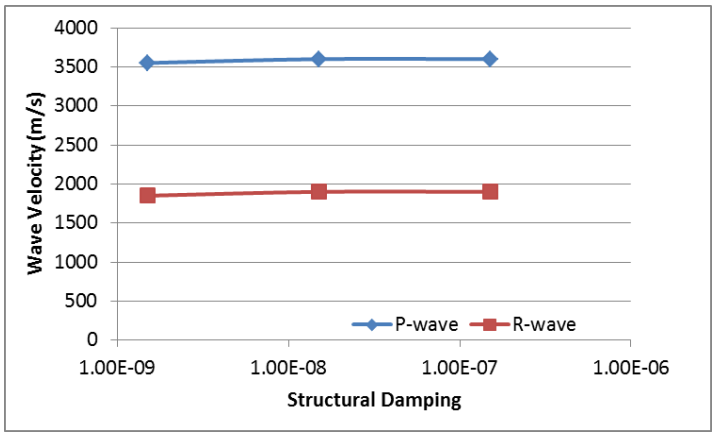

(b)

Figure 10. (a) Amplitudes and (b) wave velocities against structural damping (stiffness damping multiplier, β) in logarithmic scale from FEM simulation

4.4 Actuation Waveform

Five types of actuation waveform, in the form of sinusoidal tone burst, with 1-peak, 3-peaks, 5-peaks, 7-peaks and 9-peaks are simulated using the FEM. The actuation waveform and the sensor's electrical signature for all five types of waveform are presented in Figure 11 (a) to (e). Note that the sensor's signatures plotted in the figure are amplified by 150 times for ease of comparison with the actuation signatures.

Referring to Figure 11 (a) and (b), when the input waveform has less than 5-peaks, the wave packets for P-wave and R-wave cannot be clearly identified. On the other hand, when the numbers of peaks are increased to 7 or above, the complexity of waveform distorts the signal due to boundary reflections, which increases the difficulty of determining the TOF of both wave packets. The use of 5-peaks tone burst is recommended when performing the WP technique, which often yields clearer wave packets for both P-wave and R-wave. This conclusion is in line with the experimental counterpart, presented in Lim *et al.* (2017).

The wave velocities obtained from FE simulation are also compared to the experiment (Lim *et al.*, 2017), as graphically presented in Figure 12. The FE results match the experimental results satisfactorily.

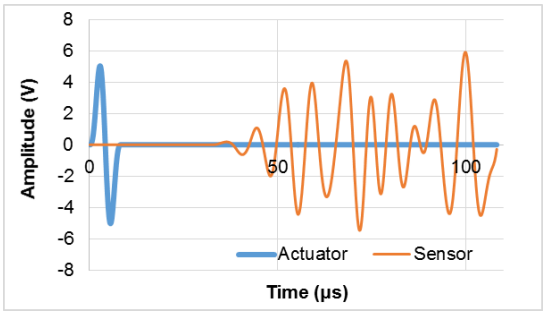

(a) 1-peak burst tone

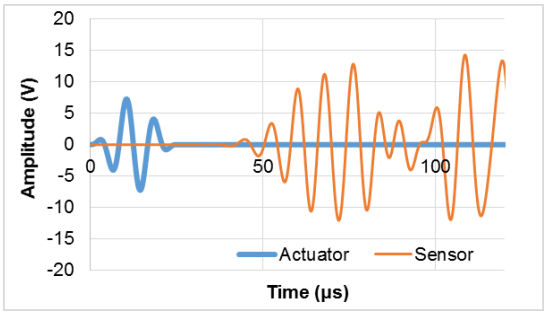

(b) 3-peaks tone burst

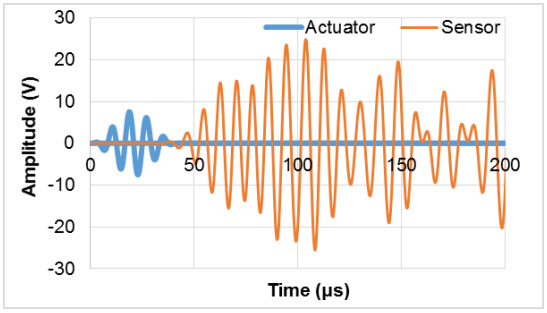

(c) 5-peaks tone burst

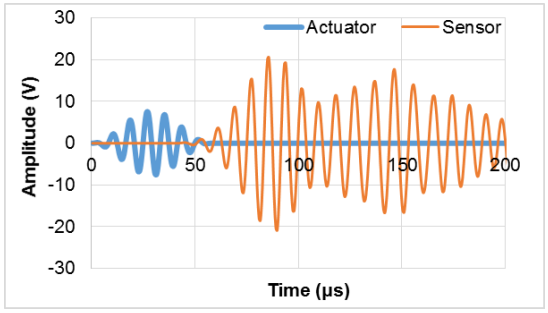

(d) 7-peaks tone burst

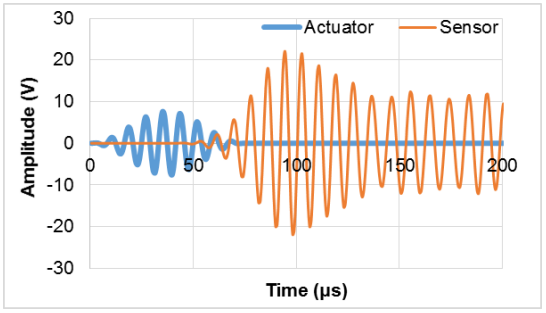

(e) 9-peaks tone burst

Figure 11. Electrical signatures against time (Sensor's signatures amplified) with various input waveform from FE simulation (1 – 9 peaks)

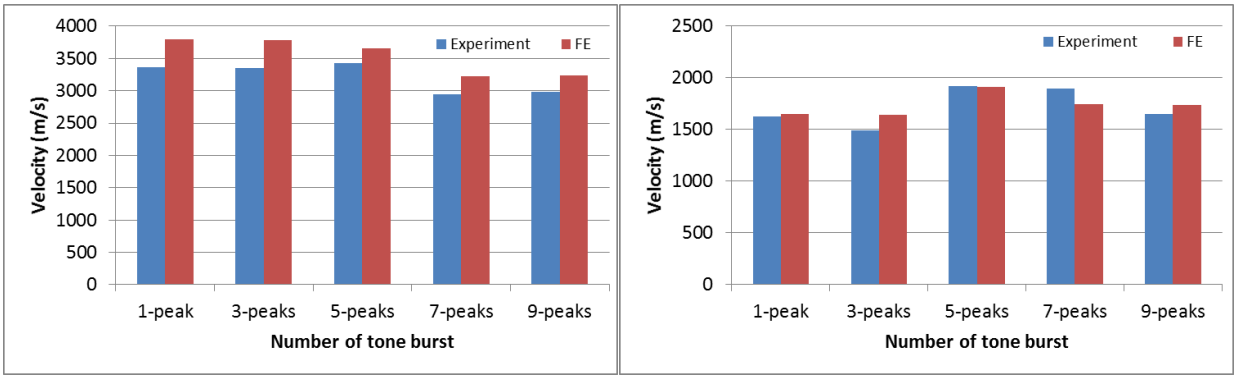

(a) (b)

Figure 12. A comparison of (a) P-wave (b) R-wave velocities calculated from various input waveforms between experiment and FE simulation

4.5 Frequency Selection

Typical actuator signals at 50 kHz, 80 kHz, 100 kHz and 120 kHz, respectively, has been simulated to investigate the effect of actuation frequency on sensor's signatures. The outcomes, in terms of electrical signature's waveform, are presented in Figure 13.

The trends of the FE simulations are found to be similar to the experimental results presented in Figure 6(b) of Lim *et al.* (2017). The signals' wave pattern at 100 kHz and 120 kHz display clearer waveforms, in comparison to the other frequency, in which P-wave and R-wave packets can be easily identified. Visually, sensor's wave patterns from other frequency range are relatively unclear.

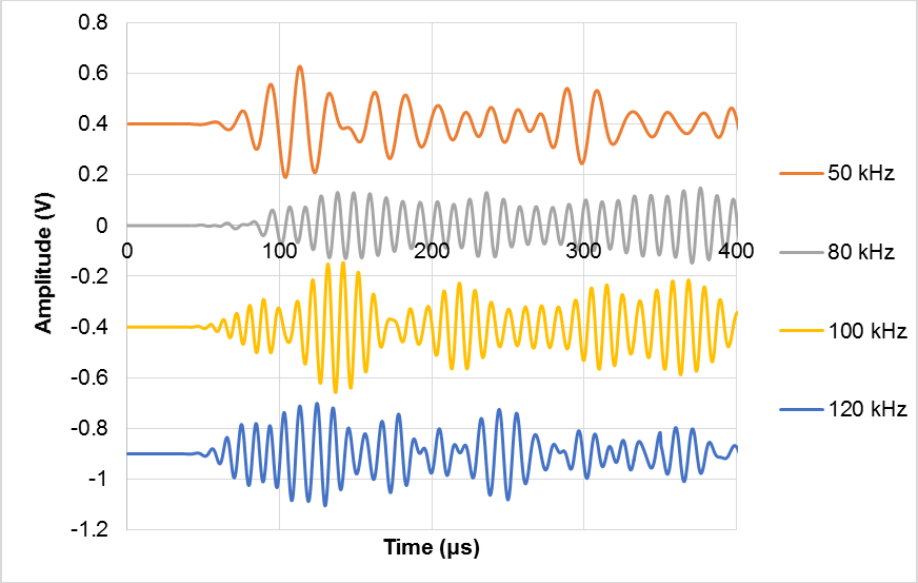

Figure 13. Sensor's electrical signatures with various actuation frequencies (50 kHz - 120 kHz) from FE simulation

4.6 Effect of Temperature and Humidity

Variations in temperature and humidity throughout a construction process are inevitable. An effective monitoring system should take into account such variations. In this section, the effects of varying temperature and humidity on the sensor's electrical signatures are experimentally investigated. Two concrete prisms, sized 100 mm x 100 mm x 500 mm, each attached with two surface bonded PZT patches were prepared for the temperature and the humidity tests. Two PZT transducers of PI Ceramics sized 15 mm x 15 mm x 0.25 mm were surface bonded on one of the smooth surface of the prisms. They are denoted as Specimen T and Specimen H respectively.

For each specimen, a baseline signature is taken with ambient temperature at 23^0C and relative humidity at 50%. The experimental setup and other details was the same as those presented in Section 3.1 of Lim *et al.* (2017).

4.6.1 Temperature

Specimen T was first placed in a fridge and thereafter inside an oven. Temperature was progressively increased from 5 ^{0}C, to room temperature (21 ^{0}C), and to 30 ^{0}C, 40 ^{0}C, 50 ^{0}C, 60 ^{0}C and 80 ^{0}C. At each step, the temperature was maintained for 30 minutes before signature acquisition commenced.

The amplitudes of the sensor's electrical signatures and the P-wave and R-wave velocities are plotted against temperature, as schematically presented in Figure 14. When the temperature is reduced from ambient temperature to 5 ^{0}C, the velocities of both waves and the amplitudes increase. In contrast, when the temperature is raised, the velocities and amplitudes decrease.

In terms of the amplitude, the raise in temperature "soften" the bonding layer, thus reducing the efficiency of energy transfer from the PZT transducer to the concrete structure. In other words, the elastic wave generated in the concrete specimen is weaker, which correspondingly reduces the amplitude of the sensor's signature. The drop in amplitude is very significant as temperature exceeds 30 ^{0}C.

In terms of the velocity, it can be explained by the fact that, the concrete become "softer" (reduction in stiffness) as the temperature increases, which is indirectly reflected from the reduction in wave velocities. The effect is more pronounced as temperature exceeded 60 ^{0}C, as a sudden decrease in gradient is observed.

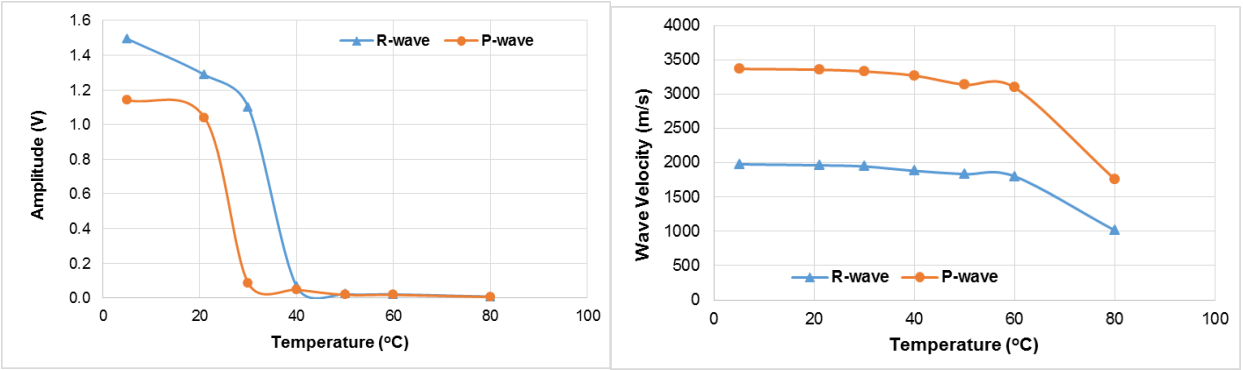

(a) (b)

Figure 14. (a) Amplitudes (b) wave velocities against temperature acquired from Specimen T

4.6.2 Humidity

To study the effect of humidity, Specimen H was kept inside a temperature and humidity control chamber. Humidity levels at 10 %, 40 %, 50 % and 90 % at constant temperature (23 ^{0}C) were tested. For each step, the humidity level was maintained for at least 6 hours before signatures were recorded.

In general, varying the level of humidity has negligible effect on both the wave velocities and the amplitude of sensor's signatures as depicted in Figure 15. The amplitude of the signatures slightly reduces when the humidity is high, which is likely to be due to the increase in damping as a result of higher moisture content in the concrete. The bonding layer is also expected to soften with higher moisture content, which reduces the efficiency of strain transfer. The increase in damping, however, has negligible effect on the wave velocity, which aligns with the structural dynamic theory.

Therefore, in general, compensation factor for humidity will not be required. However, if the concrete is exposed to high humidity (> 90 %) for prolonged period of time, further hydration

may occur, which could increase the velocities of the waves. In addition, the durability of the adhesive under sustained moisture should also be separately investigated.

In this study, no protection was provided to the PZT transducer. The patch was in direct contact with the moisture in the air. It can be shown that short term exposure to moisture does not degrade the performance of the transducer. However, for long term application, protective layer should be applied across the PZT transducer to enhance its durability.

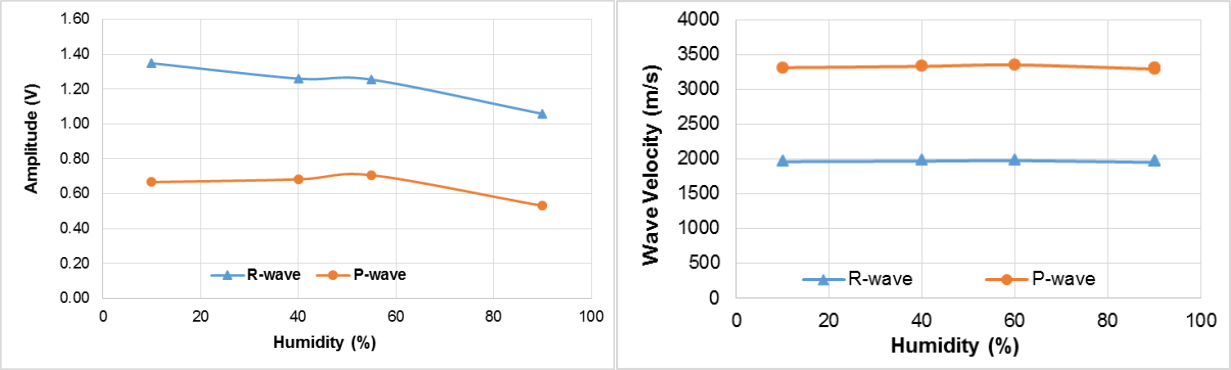

(a) (b)

Figure 15. (a) Amplitudes (b) Velocities of P-wave and R-wave versus humidity acquired from Specimen H

4.6.3 Effect on dynamic modulus of concrete

In this section, Equation (1) and (2) are used to evaluate the dynamic modulus of Specimen T at various temperature. Figure 16 shows the changes in modulus of elasticity with temperature of Specimen T. The modulus of elasticity reduces with increase in temperature. A sudden drop in elastic modulus is observed from 60^0C to 80^0C. The opposite effect is noticed when the temperature is reduced. The trend of this curve resembles the trend of both P-wave and

R-wave velocities (Figure 14b). This outcome once again shows that the wave velocities are good indicators of the stiffness of the concrete structure.

It is worth mentioning that the properties of the PZT transducer can also be altered by the change in temperature. However, according to Yang *et al.* (2008), it would mainly affect the amplitude of the signatures but not the velocities of the waves. In this application, since the wave velocities is the governing parameter, compensation technique should be developed to account for fluctuating temperature in a construction site, especially if temperature is expected to exceed 50^0C.

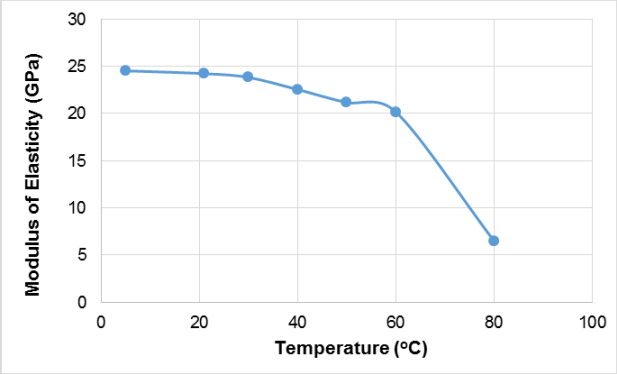

Figure 16. Modulus of elasticity versus temperature derived from Specimen T

4.7 Strength Prediction Model for different coarse aggregate

In this section, the semi-analytical model presented in Section 2 (Equation 1 to Equation 4) is adopted to produce strength calibration chart for concrete with different coarse aggregate, as presented in Section 4.10 of Lim *et al.* (2017).

Lim *et al.* (2017) experimentally investigate the effect of different types of coarse aggregate on the velocities of wave packets. Three specimens of same water-cement ration (0.4) were prepared. Specimen CaS uses river sandstone as coarse aggregate and Specimen CaG uses

granite as coarse aggregate. Specimen CaM, acting as a control, is a mortar specimen with the same cement to sand mix ratio but with no coarse aggregate. They find that the velocities of both P-wave and R-wave reflect the strength of the specimens, where stronger specimens yield higher velocity.

Using the wave velocities obtained from Lim *et al.* (2017) and following the procedures proposed by Lim *et al.* (2016), the dynamic modulus of elasticity is first evaluated, which is then followed by the establishment of the strength calibration chart.

The predicted dynamic modulus against curing time is presented in Figure 17. The trend of all three specimens resembles the wave velocities and the actual strength. The dynamic modulus of CaG is higher than CaS; and the concrete specimens (CaG and CaS) are larger than the mortar specimen (CaM). Physically, concrete with granite as aggregate is expected to be stronger than the one with sandstone, as granite is mechanically stronger than sandstone. Furthermore, both concrete specimens with coarse aggregate are no doubt stronger than the mortar specimen.

In general, concrete with higher compressive strength is stiffer (higher dynamic modulus) than those with lower strength, which can be indirectly reflected from the wave velocities. Elastic wave travels at higher speed in stiffer medium.

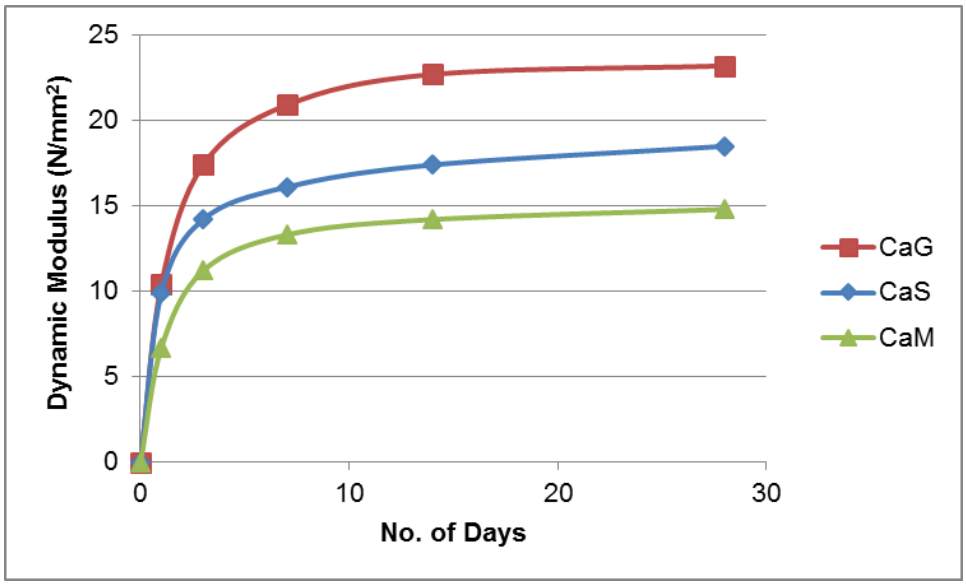

Figure 17. Dynamic modulus versus number of curing days of specimens with different coarse aggregate

A strength calibration chart, using the R-wave velocity as the indicator is constructed based on the semi-analytical model (Section 2) and presented in Figure 18. Results show that the WP technique is an effective tool for strength monitoring of concrete not only with different mix proportion (Lim *et al.*, 2016) but also with different types of coarse aggregate.

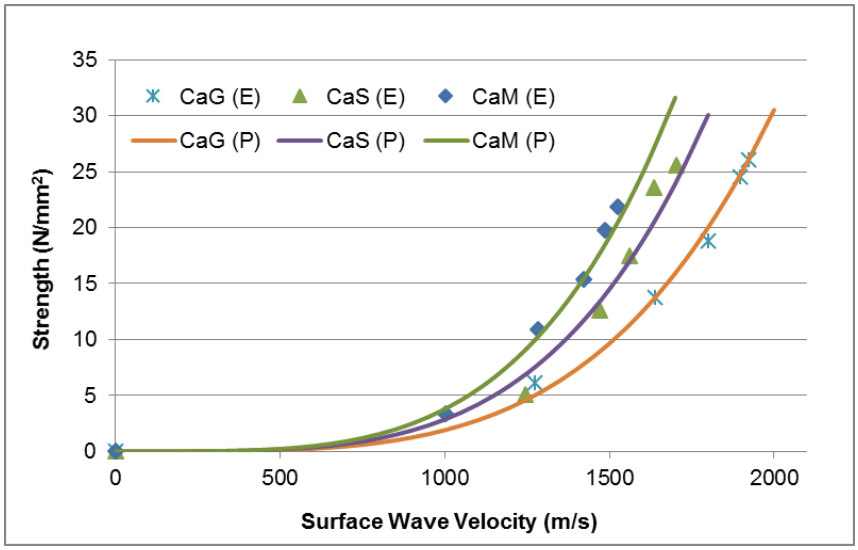

Figure 18. Strength calibration chart on concrete and mortar based on WP technique using R-wave velocity (E: Experiment, P: Prediction)

5. Conclusion

This paper is an extension of various experimental studies presented in one of the authors' recent publication. A series of parametric and numerical studies are conducted into various issues related to the practical application of the wave propagation (WP) technique in monitoring of concrete curing, using smart PZT.

FE model simulating the PZT-structure interaction of WP technique has been developed. Attempt has been made to identify the numerically simulated P-wave and R-wave. All outcomes are experimentally verified.

Parametric study using FEM and theoretical wave equations are also performed to complement the experiments conducted in the previous paper, as well as to investigate those factors uncontrollable in the experiment, including dynamic modulus of elasticity, Poisson's ratio and damping. Further experimental studies on the effect of varying environmental factors

are presented. Strength calibration chart for concrete with different coarse aggregates are generated using the previously proposed semi-analytical model.

Future study could focus on in-depth investigations into all issues presented in this paper. Attempts could be made to establish a range of modification factors for the semi-analytical model to take into account of these issues. This paper is expected to serve as a corner stone for future in-depth study and as a path forward to large-scale commercialization of this technique.

The authors wish to thank the Ministry of Higher education, Malaysia for funding this project (Fundamental Research Grant Scheme FRG0362-TK-1/2014)

6. References

ACI Committee: 228.2R. (1998). Nondestructive test methods for evaluation of concrete in structures. American Concrete Institute, Farmington Hills, Michigan.

Annamdas, V. G. and Radhika, M. A. (2013). Electromechanical impedance of piezoelectric transducers for monitoring metallic and non-metallic structures: A review of wired, wireless and energy-harvesting methods. *Journal of Intelligent Material Systems and Structures*, 1045389X13481254.

Annamdas, V. G. M. and Soh, C. K. (2007). Three-dimensional electromechanical impedance model. I: Formulation of directional sum impedance. *Journal of Aerospace Engineering*, 20(1), 53-62.

Annamdas, V.G.M. and Soh, C.K. (2009). Application of electromechanical impedance technique for engineering structures: review and future issues. *Intell. Mater. Syst. Struct.*, 21, 41-59.

Balendra, S. (2005). Numerical modeling of dynamic soil–pile–structure interaction. *MS Thesis*, Washington State University.

Bhalla, S., and Soh, C. K. (2004). Structural health monitoring by piezo-impedance transducers. I: Modeling. *Journal of Aerospace Engineering*, 17(4), 154-165.

British Standard: 8110. (1985). Structural use of concrete Part 2: Code of practice for special circumstances. British Standards Institution.

Djemana, M., & Hrairi, M. (2016). Modelling and simulation of impedance-based damage monitoring of structures. *International Journal of Simulation Modelling*, 15(3), 395-408.

Giurgiutiu, V. (2005). Tuned Lamb wave excitation and detection with piezoelectric wafer active sensors for structural health monitoring. *Journal of intelligent material systems and structures*, 16(4), 291-305.

Giurgiutiu, V. (2007). Structural health monitoring: with piezoelectric wafer active sensors. Academic Press.

Giurgiutiu, V. and Zagrai, A. N. (2000). Characterization of piezoelectric wafer active sensors. *J. Intell. Mater. Syst. Struct.*, 11, 959–76.

Giurgiutiu, V., Zagrai, A. and Bao, J. J. (2002). Piezoelectric wafer embedded active sensors for aging aircraft structural health monitoring. *Structural Health Monitoring*, 1(1), 41-61.

Gresil, M., Yu, L., Giurgiutiu, V. and Sutton, M. (2012). Predictive modeling of electromechanical impedance spectroscopy for composite materials. *Structural Health Monitoring*, 11(6), 671-683.

Gu, H., Song, G., Dhonde, H., Mo, Y. L. and Yan, S. (2006). Concrete early-age strength monitoring using embedded piezoelectric transducers. *Smart Mater. Struct*.,15, 1837-1845.

Jones, R. (1962). Non-destructive testing of concrete. Cambridge University Press. London

Kijanka, P., Packo, P., Zhu, X., Staszewski, W. J. and Scalea, F. L. (2015). Three-dimensional temperature effect modelling of piezoceramic transducers used for Lamb wave based damage detection. *Smart Materials and Structures*, 24(6), 065005.

Kong, Q., Hou, S., Ji, Q., Mo, Y. L., and Song, G. (2013). Very early age concrete hydration characterization monitoring using piezoceramic based smart aggregates. *Smart Materials and Structures*, 22(8), 085025.

Kong, Q. and Song, G. (2017). A comparative study of the very early age cement hydration monitoring using compressive and shear mode smart aggregates. *IEEE Sensors Journal*, 17(2), 256-260.

Liang, C., Sun, F. P. and Rogers, C. A. (1996) Electro-mechanical impedance modelling of active material systems. *Smart Mater. Struct*., 5, 171–86.

Lim, Y. Y., Kwong, K. Z., Liew, W. Y. H., & Soh, C. K. (2016). Non-destructive concrete strength evaluation using smart piezoelectric transducer—a comparative study. *Smart Mater. Struct.*, 25(8), 085021.

Lim, Y.Y., Kwong, K.Z., Liew, W.Y.H. and Soh, C.K. (2017). Practical issues related to the application of Piezoelectric based propagation technique in monitoring of concrete curing. *Construction and building Materials*, 152, 506-519.

Lim, Y.Y. and Soh, C.K. (2011). Fatigue life estimation of a 1D aluminum beam under mode-I loading using electromechanical impedance technique. *Smart Mater. Struct*. 20, 125001.

Lim, Y. Y. and Soh, C. K. (2012). Effect of varying axial load under fixed boundary condition on admittance signatures of electromechanical impedance technique. *J. Intell. Mater. Syst. Struct.*, 23, 815–826.

Lim, Y. Y. and Soh, C. K. (2014). Towards more accurate numerical modeling of impedance based high frequency harmonic vibration. *Smart Materials and Structures*, 23(3), 035017.

Liu, W. and Giurgiutiu, V. (2007). Finite element simulation of piezoelectric wafer active sensors for structural health monitoring with coupled-field elements. *Proc. SPIE*, 6529, 6529–125.

Lu, X., Lim, Y. Y., and Soh, C. K. (2017). A novel electromechanical impedance–based model for strength development monitoring of cementitious materials. *Structural Health Monitoring*, 1475921717725028.

Lu, X., Lim, Y. Y., and Soh, C. K. (2018). Investigating the performance of "Smart Probe" based indirect EMI technique for strength development monitoring of cementitious materials – Modelling and parametric study. Construction and Building Materials. (172), 134-152.

Luo, W. and Rose, J. L. (2007). Phased array focusing with guided waves in a viscoelastic coated hollow cylinder. *J. Acoust. Soc. Am*., 121, 1945–55.

Moulin, E., Assaad, J., Delebarre, C. and Osmont, D. (2000). Modeling of Lamb waves generated by integrated transducers in composite plates using a coupled finite element--normal modes expansion method. *The Journal of the Acoustical Society of America*, 107(1), 87-94.

PI Ceramic. (2016). *Product Information Catalogue*, Germany: Lindenstrabe.

Shin, S. W., Qureshi, A. R., Lee, J. Y. and Yun, C. B. (2008). Piezoelectric sensor based non-destructive active monitoring of strength gain in concrete. *Smart Mater. Struct*. 17, 055002.

Song, F., Huang, G. L., Kim, J. H. and Haran, S. (2008). On the study of surface wave propagation in concrete structures using a piezoelectric actuator/sensor system. *Smart Mater. Struct*., 17, 1-8.

Tian, Z., Huo, L. S., Gao, W. H., Li, H. N. and Song, G. B. (2017). Modeling of the attenuation of stress waves in concrete based on the Rayleigh damping model using time-reversal and PZT transducers, *Smart Mater. Struct.*, 26(10): 105030.

Wang, D., Song, H. and Zhu, H. (2014). Embedded 3D electromechanical impedance model for strength monitoring of concrete using a PZT transducer. *Smart Materials and Structures*, 23(11), 115019.

Wang D. S. and Zhu H. P. (2011). Monitoring of the strength gain of concrete using embedded PZT impedance transducer, *Construction and Building Materials*, 25(9): 3703-3708.

Wu, F. and Chang, F. K. (2006). Debond detection using embedded piezoelectric elements in reinforced concrete structures—part II: analysis and algorithm. *Struct. Health. Monit*., 5, 17–28.

Yang, Y., Lim, Y. Y. and Soh, C. K. (2008). Practical issues related to the application of the electromechanical impedance technique in the structural health monitoring of civil structures: I. Experiment. *Smart Mater. Struct*., 17, 035008.

Yu, L. (2006). In-situ structural health monitoring with piezoelectric wafer active sensor guided-wave phased arrays. PhD Thesis, University of South Carolina.